

Learning High-fidelity Light Field Images From Hybrid Inputs

Jing Jin¹, Junhui Hou¹, Jie Chen², Sam Kwong¹, and Jingyi Yu³

¹Department of Computer Science, City University of Hong Kong

²School of Electrical & Electronic Engineering, Nanyang Technological University

³School of Information Science and Technology, ShanghaiTech University

Abstract

This paper explores the reconstruction of high-fidelity LF images (i.e., LF images with both high spatial and angular resolution) from hybrid inputs, including a high resolution RGB image and a low spatial but high angular resolution LF image. To tackle this challenging problem, we propose a novel end-to-end learning-based approach, which can comprehensively utilize the specific characteristics of the input from two complementary and parallel perspectives. Specifically, one module efficiently learns a deep multi-dimensional and cross-domain feature representation to regress an intermediate estimation; the other one propagates the information of the input, which is challenging to predict, to construct another intermediate estimation. We finally leverage the advantages of the two intermediate estimations via the learned confidence maps, leading to the final high-fidelity LF image. Extensive experiments demonstrate the significant superiority of our approach over the state-of-the-art ones. That is, our method not only improves the PSNR more than 2 dB, but also preserves the LF structure much better. To the best of our knowledge, this is the first end-to-end deep learning method for reconstructing a high-fidelity LF image with a hybrid input. We believe our framework could potentially decrease the cost of high-fidelity LF data acquisition and also be beneficial to LF data storage.

1. Introduction

The light field (LF) describes all light rays through every point along every direction in a free space [24]. An LF image can be interpreted as multiple views observed from viewpoints regularly distributed over a 2-D grid. Therefore, LF images contain not only color information but also geometric structure of the scene in an implicit manner. The rich information enables many applications such as mate-

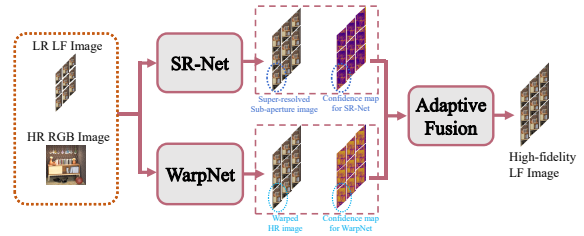


Figure 1. The flowchart of the proposed approach. Two modules are involved. SR-Net spatially super-resolves the input LR LF under the guidance of the HR RGB image, and WarpNet warps the input HR RGB image with the disparity maps estimated from the LR LF image. Finally, the predictions produced by these two modules are adaptively fused based on the learned confidence maps to generate a high-fidelity LF image. Note that an LR LF image denotes an LF image with low spatial but high angular resolution. The spatial resolution of an LF image refers to the spatial resolution of its sub-aperture images.

rial recognition [35], saliency detection [25], motion deblurring [31], image post-refocusing [10], and 3D reconstruction [20]. Recent research also demonstrates that LF is a promising media for virtual/augment reality [15, 45].

With the availability of commodity LF cameras such as Lytro and Raytrix [1, 2, 29], an LF image can be conveniently acquired in a single shot. For such kind of LF cameras, there is an inherent trade-off between the spatial and angular resolution. Due to limited sensor resolution, the captured LF images always suffer from low spatial resolution, which severely limits its practical applications. To overcome this limitation, many methods for reconstructing high-fidelity LF images (i.e., LF images with both high spatial and angular resolution) have been proposed [42, 30, 44, 43, 4, 37, 48, 39]. Among them, LF reconstruction with a hybrid input is a promising way. Typically, a hybrid LF imaging system consists of a plenoptic camera and a traditional DSLR camera [4, 36], and various prototypes were proposed, such as arranging several low-

cost lens around a DSLR camera [39] or placing a beam splitter to separate the light rays from the object [37]. In the hybrid imaging system, a low-resolution (LR) 4-D LF image, as well as a high-resolution (HR) 2-D RGB image, are captured simultaneously. The LR LF image is mainly responsible for recording the geometry information of the scene, while the HR RGB image contains delicate textures and high-frequency information of the scene. To produce a high-fidelity LF image, a post-process algorithm is necessary to combine the information of the two types of images.

Multiple algorithms have been proposed to reconstruct a high-fidelity LF from the hybrid input. However, existing methods [4, 37, 48, 39] still have limited performance. Generally, these methods comprise several steps that are independently designed, and the final results would be compromised by any inaccuracy of each step. Furthermore, these methods fail to fully describe the complicated relation between the LR LF image and the HR RGB image as well as the one within the high-dimensional LF image.

Our Contributions. We propose a learning-based framework to reconstruct a high-fidelity LF image with a hybrid input in an end-to-end manner. To the best of our knowledge, this is the first one. The proposed framework produces impressive performance. As illustrated in Fig. 1, in contrast to existing ones, our framework achieves the goal with two *complementary* and *parallel* research lines, namely SR-Net and WarpNet. The SR-Net adopts the general idea of image super-resolution and up-samples the LR LF image to the desired resolution by learning a deep representation from both components of the hybrid input. This module is able to maintain the spatial and angular consistency from the LR LF image, but the results are always blurred, especially when the up-sampling scale is relatively large. In WarpNet, the HR RGB image is warped to synthesize an HR LF using the disparity/depth maps estimated from the LR LF. The predictions by this module inherit the delicate textures and high-frequency information from the HR RGB image, but always have artifacts caused by occlusion or disparity inaccuracy. Observing the complementary behavior between these two modules, we learn a pixel-wise confidence map for the output of each module. And, the final high-fidelity LF image is obtained by adaptively fusing the two intermediate predictions based on their confidence maps, in which only their advantages are collected.

2. Related Work

LF Image Super-resolution. Single image super-resolution (SISR) is a classical problem in the field of image processing. To solve this ill-posed inverse problem, lots of regularization based methods [16, 5, 33] have been proposed. Recently deep learning based methods [7, 21, 22, 47, 18, 23] have achieved great success. We refer the reader to [32, 40] for comprehensive review on SISR.

Different from SISR, LF image super-resolution aims at simultaneously increasing the spatial resolution of all sub-aperture images (SAIs) in an LF image. On top of the target to recover high-frequency details for each SAI, LF super-resolution should also maintain the LF structure. To characterize the relation between SAIs, many methods define a physical model to reconstruct the observed LR SAIs using the desired HR ones. Afterwards, the inverse problem is solved by different priors [28, 42, 11, 30]. These methods always require accurate disparity estimation.

Recent years have witnessed progress on learning-based methods for LF super-resolution. Farrugia *et al.* [8] constructed a training set by 3D-stacks of 2-D-patches cropped from different SAIs of paired LF images, and then learned a linear mapping between the subspace of the LR and HR patch stacks. Yoon *et al.* [44] are the first to apply convolutional neural network (CNN) on LF images. However each SAI of an LF image is processed independently in their network, which neglects the angular relationship. Therefore, Yuan *et al.* [46] proposed to refine the result after separately applying an SISR approach on each SAI. They designed an enhancement network to restore the continuous line structures in the extracted epipolar plane images (EPIs). For the same purpose of keeping the geometric consistency in the reconstructed LF image, Wang *et al.* [38] adopted a recurrent neural network to learn the relations between adjacent SAIs along horizontal and vertical directions. To take advantage of the complementary information between SAIs introduced by the LF structure and address the high-dimensionality challenging, Yeung *et al.* [43] proposed to use 4-D convolution and more efficient spatial-angular separable convolution on LF images, which achieves the state-of-the-art performance.

LF Image Super-resolution with a Hybrid Input. LF hybrid imaging system was first proposed by Lu *et al.* [26], in which an HR RGB camera is co-located with a Stack-Hartmann sensor. Boominathan *et al.* [4] proposed a patch-based method named *PaSR* to improve the resolution with the hybrid input. Based on *PaSR*, Wang *et al.* [39] improved the performance by iterating between patch-based super-resolution and depth-based synthesis, where the synthesized images were used to update the patch dictionary. The patch-based approaches avoid the need to calibrate and register the DSLR camera and the LF camera. However, the average aggregation causes blurring. Zhao *et al.* [48] proposed to separate the high-frequency details from the HR image and warp them to all SAIs to reconstruct an HR LF image. A similar but simpler task is reference-based SISR. Zheng *et al.* [49] designed a network, named *CrossNet*, to align the information of an HR image to the target LR image which is captured from a different viewpoint. Besides spatial super-resolution, the hybrid LF imaging system was also used to generate LF videos [36].

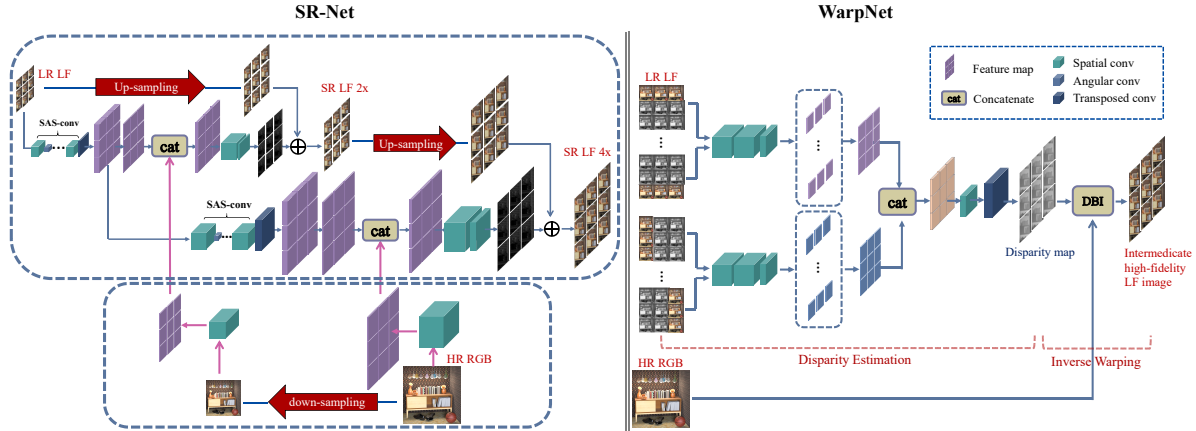


Figure 2. Illustration of the network architectures of the SR-Net (left) and WarpNet (right). The SR-Net progressively super-resolves the LR LF in a coarse-to-fine manner, and the information from the HR RGB image is progressively extracted and brought in along an inverse direction. Note that the left figure illustrates the SR-Net of $4\times$ reconstruction, and the model for a larger scale can be realized by cascading more levels. The WarpNet first estimates and spatially super-resolves the 4-D disparity maps from the LR LF, and then warps the HR RGB image to synthesis an intermediate high-fidelity LF image. *DBI* stands for the Differentiable Bicubic Interpolation.

3. The Proposed Approach

3.1. Overview

Let $L^l(x, y, s, t)$ ($1 \leq x \leq W, 1 \leq y \leq H, 1 \leq s \leq M, 1 \leq t \leq N$) denote an LR 4-D LF image of spatial resolution $W \times H$ and angular resolution $M \times N$. A high-fidelity 4-D LF image to be reconstructed is denoted as $\tilde{L}^h(x', y', s', t')$ ($1 \leq x' \leq \alpha W, 1 \leq y' \leq \alpha H, 1 \leq s' \leq M, 1 \leq t' \leq N$), where $\alpha > 1$ is the up-sampling scale factor, and the corresponding ground-truth one is denoted as I^h . An HR 2-D RGB image of resolution $\alpha W \times \alpha H$ is denoted as I^h . The problem of reconstructing \tilde{L}^h from the given L^l and I^h can be implicitly formulated as

$$\tilde{L}^h = \mathcal{F}(L^l, I^h). \quad (1)$$

Considering the powerful representation ability of deep CNNs, we investigate a deep neural network that can well capture the characteristics of the input to learn such a mapping function \mathcal{F} .

To reconstruct high-fidelity \tilde{L}^h , the specific properties of the hybrid input L^l and I^h have to be fully explored. As shown in Fig. 1, our approach consists of two modules, namely SR-Net and WarpNet. More specifically, by efficiently learning deep representations from both L^l and I^h , the SR-Net aims to super-resolve L^l in a progressive manner (i.e., to equally increase the spatial resolution of all SAIs contained in L^l), leading to an intermediate high-fidelity LF image and its corresponding confidence map. The WarpNet learns another intermediate high-fidelity LF image as well as its confidence map, in which I^h is inversely warped with the disparity estimated from L^l . Finally, the two intermediate predictions are adaptively fused based on the learned

confidence maps such that only their respective advantages can be combined into a better output. Note that our approach is trained end-to-end. In the following, the details of the proposed approach as well as comprehensive analyses are presented step-by-step.

3.2. SR-Net

As depicted in Fig. 2, the SR-Net is composed of two branches, i.e., an up-sampling branch used to progressively up-sample L^l , and a down-sampling branch used to progressively extract features from I^h . The two structurally opposite branches are connected to promote sufficient exploration of the information contained in the hybrid input.

The Up-sampling Branch. The high dimensionality of LF data makes it memory and time consuming for convolutional operations. To address this challenging issue, we adopt a cascaded hourglass structure [22, 43], which sequentially extract features at the LR level and recursively up-samples L^l . Specifically, L^l is super-resolved at $\log_2 \alpha$ levels. At each level, the LR input goes through a group of spatial-angular separable convolutional (*SAS-conv*) layers and a learnable transposed convolutional layers, and a residual map for the up-sampled image is finally learned using the features extracted by prior convolutions from both L^l and I^h .

Different from single images, SAIs in an LF image are not independent but have an implicit relation, i.e., LF structure. Specifically, under the Lambertian assumption and in the absence of occlusions, such a relation can be expressed as

$$L^l(x, y, s, t) = L^l(x + d\Delta s, y + d\Delta t, s + \Delta s, t + \Delta t), \quad (2)$$

where d is the disparity of the pixel located at (x, y, s, t) . Such a relation yields the complementary information between SAIs (i.e., details absent at a certain SAI may be present in another one), which may be beneficial to the reconstruction quality. Therefore, to take advantage of this valuable information in L^l , we use the computationally efficient *SAS-conv* [43] at each level to achieve the sequential feature extraction, in which 2-D convolutional layers are performed alternatively on the spatial and angular domain. The features extracted by *SAS-conv* at each level will be fed into two paths: one path will be combined with the feature extracted from I^h for residual prediction at the current level; the other path will be fed as input for feature extraction at the next level. In addition, the high-capacity of a CNN model has the potential ability to handle the non-Lambertian surfaces/reflectance always occurring in practice, under which the relation in Eq. 2 no longer holds.

The Down-sampling Branch. As mentioned before, the HR RGB image included in the hybrid input embeds rich information of the scene, i.e., high-frequency information and delicate textures. This branch aims to borrow this property to enhance the learning ability of the up-sampling branch. In this branch, we progressively extract features from I^h along an orientation opposite to the up-sampling branch. Specifically, at the k -th level ($k = 0, \dots, \log_2 \alpha - 1$), I^h is first down-sampled to the size of $2^{-k} \alpha W \times 2^{-k} \alpha H$, and then feature maps with the same size are extracted by sequential convolutional layers. The feature maps extracted from I^h at the k -th level are concatenated to those from L^l at the $(\log_2 \alpha - k)$ level along the feature channel. The combined feature maps are further fed into the residual learning component of the up-sampling branch to reconstruct the intermediate high-fidelity LF image.

The SR-Net is trained by minimizing the absolute error between the output denoted as \tilde{L}_s^h (i.e., an intermediate high-fidelity LF images) and the ground-truth high-fidelity LF images:

$$\ell_s^p = \|L^h - \tilde{L}_s^h\|_1. \quad (3)$$

Remark. This module relies on the powerful modelling capacity of the deep CNN to super-resolve L^l for an intermediate high-fidelity LF image. By progressively combining features extracted from L^l and I^h for the learning of HR residuals, it is expected that the SR-Net can reconstruct the high-fidelity LF image as well as possible. However, its output still suffers from blurry effects, caused by convolution and ℓ_1 loss [27, 23], although I^h contains the high-frequency information of the scene. See the analysis in Sec. 4.4 and Fig. 4. In other words, the high-frequency information embedded in I^h cannot be very effectively propagated to the output of the SR-Net. To this end, we further develop the following WarpNet.

3.3. WarpNet

As illustrated in Fig. 2, there are two sub-phases involved in this module, i.e., disparity estimation and inverse warping. The WarpNet first learns an HR disparity map for each SAI by exploring the unique LF structure of L^l , which is further used to inversely warp I^h , leading to another intermediate high-fidelity LF image as well as its confidence map.

Disparity Estimation. Disparity estimation is a basic problem for LF images, which aims to estimate the relation in Eq. 2. The disparity is inversely proportional to the depth. Lots of methods [41, 34, 12, 9] have been proposed by exploiting the line structures in 2-D EPIs. Based on the insight that estimating disparities for pixels is to find their correspondences from all SAIs, we believe that a fully convolutional network has the ability to understand the LF structure, and thus estimate the disparity.

Owing to the symmetry of the SAI distribution, an LF image has the same disparity along horizontal and vertical directions. However, difficulties of inferring the horizontal and vertical disparity are different, which mostly depend on the scene content. For example, if there is a region of vertical texture, using a horizontal stack of SAIs will make it easier to deduce the disparities for pixels in this area, because pixels are not easy to be distinguished when finding their correspondences along the vertical direction. Therefore, we propose to estimate the 4-D disparity map from horizontal and vertical stacks separately.

Specifically, we first re-organize SAIs of L^l to construct N horizontal and M vertical stacks. The i -th (resp. j -th) horizontal (resp. vertical) stack contains the i -th row (j -th column) of the SAI array ($1 \leq i \leq M, 1 \leq j \leq N$). A series of convolutional layers are applied on each stack, and those stacks corresponding to the same orientation share the weights of the convolutional kernels. The output of the final layer has the size of $W \times H \times M$ and consists of the feature maps for all SAIs in each stack. By simply collecting N horizontal feature maps, we obtain the 4-D feature map denoted as D_h , which only considers the horizontal structure in L^l . Likewise, the vertical feature map D_v is computed from the vertical stacks. Finally, the final 4-D LR disparity map D^l is generated by weighted averaging the horizontal and vertical feature maps, i.e.,

$$D^l = w_1 D_h + w_2 D_v, \quad (4)$$

where the weights w_1 and w_2 are adaptively learned through a convolutional layer with a kernel of size 1×1 . Note that the 4-D disparity map D^l estimated from L^l has the same spatial resolution as L^l . However, to warp I^h , an HR disparity map that has the same spatial resolution as I^h is necessary. Considering the fact that the disparity map represents geometric information, which usually has much simpler patterns than the corresponding color image, we be-

lieve it is much easier to up-sample D^l than L^l . Therefore, we up-sample D^l with learnable transposed convolutional layers, leading to the HR 4-D disparity map denoted as D^h .

Inverse Warping. Based on D^h , another intermediate high-fidelity LF image can be synthesized by inversely warping I^h to each viewpoint. To make this module to be end-to-end trainable, we employ the differentiable bicubic interpolation [17] to realize the process of inverse warping.

To train the WarpNet, we minimize the absolute error between the synthesized high-fidelity LF image \tilde{L}_w^h and its ground-truth, i.e.,

$$\ell_w^p = \|L^h - \tilde{L}_w^h\|_1. \quad (5)$$

Remark. By reusing pixels from I^h , we expect the high-frequency details of the scene that are challenging to predict can be directly transferred from I^h to each SAI of \tilde{L}_w^h . For example, for regions with continuous depths and complicated textures, WarpNet performs quite well. See the visual results in Fig. 4. However, \tilde{L}_w^h inevitably has distortion caused by inaccurate disparity estimations or occlusions. Specifically, it is difficult to obtain accurate disparities without the ground-truth disparities for supervision, especially in challenging regions, such as textureless regions. Such inaccurate disparities will warp pixels of I^h to wrong positions, resulting in distortion. Second, pixels observed in SAIs of L^l but occluded in I^h will be occupied by the occluder after warping, causing error. Interestingly, the SR-Net suffers less from the distortion induced by these two factors. For example, the textureless regions, where the disparities cannot be accurately estimated, correspond to low-frequency contents, which can be relatively easily predicted by the SR-Net. Besides, the powerful regression ability of the SR-Net can predict the occluded pixels to some extent [19].

3.4. Adaptive Fusion

As mentioned before, the SR-Net is capable of predicting the overall content of a high-fidelity LF image but fails to recover its delicate textures and sharp edges. WarpNet is able to propagate the high-frequency information to all SAIs but suffers from the distortion caused by occlusions and inaccurate disparity estimation. Fortunately, their advantages are complementary to each other. Therefore, a high-fidelity LF image can be finally reconstructed by adaptively fusing \tilde{L}_s^h and \tilde{L}_w^h , in which their advantages are leveraged. And such an adaptive fusion process is achieved under the guidance of their own pixel-wise confidence maps.

Both confidence maps are learned from the features extracted by SR-Net and WarpNet. In SR-Net, an additional layer parallel to the output layer at the last level is used to generate the 4-D confidence map denoted as C_s . The loss

function for training this layer is defined as:

$$\ell_s^c = \frac{1}{P} \sum_{x,y,s,t} (l^h - \tilde{l}_s^h)^2 \cdot \frac{c_s}{\|C_s\|_2}, \quad (6)$$

where P is the total number of pixels. l^h , \tilde{l}_s^h and c_s are the pixels at (x, y, s, t) in L^h , \tilde{L}_s^h and C_s , respectively. In WarpNet, similar to the disparity estimation, the network first produces a horizontal and a vertical confidence maps, which are then merged to predict the one corresponding to \tilde{L}_w^h , denoted as C_w . The up-sampling operation is also performed by transposed convolutional layers. The objective ℓ_w^c is defined the same way as ℓ_s^c .

To produce the final reconstruction \tilde{L}^h , we first apply a Softmax normalization across C_s and C_w , generating \tilde{C}_s and \tilde{C}_w , then weighted sum \tilde{L}_s^h and \tilde{L}_w^h :

$$\tilde{L}^h = \tilde{L}_s^h \odot \tilde{C}_s + \tilde{L}_w^h \odot \tilde{C}_w, \quad (7)$$

where \odot is the element-wise multiplication operator. Such an adaptive fusion process is trained under the supervision of minimizing the ℓ_1 distance between the final reconstructed high-fidelity LF image and the ground truth one:

$$\ell^p = \|L^h - \tilde{L}^h\|_1. \quad (8)$$

Combining all modules, the whole network is trained end-to-end with the following loss function:

$$\ell = \lambda_1 \ell^p + \lambda_2 \ell_s^p + \lambda_3 \ell_s^c + \lambda_4 \ell_w^p + \lambda_5 \ell_w^c, \quad (9)$$

where all values of the weight factors $\lambda_1, \dots, \lambda_5$ are empirically set to 1. Please refer to the *Supplementary Material* for the detailed settings of our network.

4. Experiments

4.1. LF Data Augmentation

Commonly used methods for data augmentation, including image rotation and flip, are not suitable for LF data. If we apply these transformations on each SAI separately, the LF structure in Eq. 2 would be destroyed. For example, applying the flip operation along the y dimension, we have

$$\begin{aligned} &L(x, H - y, s, t) \\ &= L(x + d\Delta s, H - (y + d\Delta t), s + \Delta s, t + \Delta t) \\ &= L(x + d\Delta s, (H - y) - d\Delta t, s + \Delta s, t + \Delta t). \end{aligned} \quad (10)$$

Then the corresponding pixel of the point $L(x, H - y, s, t)$ in the $(s + \Delta s, t + \Delta t)$ -th SAI cannot be found, according to the original relationship in Eq. 2. Therefore, we propose to apply these image geometric augmentation methods on both angular and spatial dimensions. With our new strategy, taking the flip augmentation along the y dimension as an example again, we have

$$\begin{aligned} &L(x, H - y, s, N - t) \\ &= L(x + d\Delta s, H - (y + d\Delta t), s + \Delta s, N - (t + \Delta t)) \\ &= L(x + d\Delta s, (H - y) - d\Delta t, s + \Delta s, (N - t) - \Delta t), \end{aligned} \quad (11)$$

LF image	scale	Bicubic	PaSR [4]	CrossNet [49]	SAS-conv [43]	M-VDSR[43]	M-VDSR-H	Ours
Bedroom	4×	30.86/0.897	34.67/0.951	<u>38.12/0.978</u>	33.98/0.948	32.80/0.935	37.19/0.974	39.40/0.983
Boardgames	4×	27.66/0.877	34.82/0.978	<u>39.88/0.992</u>	33.51/0.962	30.45/0.929	36.64/0.980	41.65/0.993
Sideboard	4×	23.93/0.739	27.05/0.874	<u>30.15/0.940</u>	27.98/0.898	26.19/0.847	<u>30.31/0.936</u>	33.56/0.970
Town	4×	28.49/0.869	31.64/0.930	<u>37.50/0.982</u>	32.14/0.933	30.99/0.919	36.24/0.974	40.15/0.988
Avg.	4×	27.74/0.846	32.05/0.933	<u>36.41/0.973</u>	31.90/0.935	30.11/0.908	35.10/0.966	38.69/0.983
Bedroom	8×	28.29/0.844	33.39/0.937	<u>36.37/0.969</u>	30.55/0.906	29.19/0.889	34.06/0.954	37.35/0.977
Boardgames	8×	24.37/0.781	32.01/0.956	<u>35.99/0.983</u>	27.83/0.883	25.53/0.832	30.41/0.942	37.84/0.987
Sideboard	8×	21.11/0.587	24.58/0.768	<u>26.46/0.870</u>	22.99/0.746	22.00/0.711	25.92/0.858	29.27/0.932
Town	8×	25.59/0.794	29.73/0.904	<u>34.05/0.962</u>	28.13/0.880	27.06/0.865	32.09/0.945	36.09/0.974
Avg.	8×	24.84/0.752	29.93/0.891	<u>33.22/0.946</u>	27.37/0.854	25.94/0.824	30.63/0.925	35.14/0.968

Table 1. Quantitative comparisons of the proposed approach with the state-of-the-art ones over the *HCI* dataset. The best results are bolded, and the second best ones are highlighted with underlines.

scale	Bicubic	PaSR [4]	CrossNet [49]	SAS-conv [43]	M-VDSR[43]	M-VDSR-H	Ours
4×	29.08/0.888	34.01/0.963	38.47/0.986	33.02/0.948	32.41/0.943	39.10/0.985	40.22/0.988
8×	26.18/0.812	32.39/0.951	<u>37.40/0.983</u>	28.22/0.881	27.70/0.871	35.91/0.974	38.26/0.983

Table 2. Quantitative comparisons of the proposed approach with the state-of-the-art ones over the *Lytro* dataset. Here, the average values of the PSNR/SSIM over 20 LF images are reported. Please refer to the *Supplementary Material* for the PSNR/SSIM value of each testing image.

where the LF structure described in Eq. 2 is still satisfied.

4.2. Datasets and Training Details

In our experiments, following [39, 37], we simulated hybrid inputs using LF images. For each LF image, the HR center SAI was selected as the HR RGB image¹, and all SAIs of the LF image were down-sampled using bicubic interpolation to get the LR LF image.

The performance of the proposed algorithm was evaluated on both synthetic and real-world LF datasets. For the synthetic data, the 4-D LF benchmark *HCI* [13] was used, which contains 24 LF images with rich content. Each LF image has spatial resolution of 512×512 and angular resolution of 9×9 . We selected 4 LF images for test and the remaining for training. For the real-world data, we used LF images captured with a Lytro ILLum camera from Stanford Lytro LF Archive [3] and the dataset provided by [19], resulting in 130 training data and 20 testing data. In this dataset, called *Lytro*, each LF image has spatial resolution of 376×541 and angular resolution of 8×8 . Please refer to the *Supplementary Material* for more details of the datasets.

We trained the proposed network individually on the *HCI* and *Lytro* datasets. The LF images were converted to YUV color space, and only the Y components were used for training and quantitative evaluation. When generating visual results, the U and V components were up-sampled using bicubic interpolation. We used Adam as the optimizer. The learning rate was initialized as $1e-4$ and $1e-5$ for $4 \times$ and $8 \times$ reconstruction, respectively, and reduced by a half when the loss stops decreasing. The code of our method will be publicly available.

¹Note that other SAIs can also be used as the HR RGB image.

4.3. Comparisons with State-of-the-Art Methods

We compared the proposed approach with state-of-the-art methods, including *PaSR* [4], *CrossNet* [49], *SAS-conv* [43] and *M-VDSR* [43]. *M-VDSR* was developed by modifying *VDSR* [21] to adapt to LF data, in which all SAIs of an LF image are stacked along the feature channel and then fed into the network at the same time. Additionally, based on *M-VDSR*, we developed another baseline to handle a hybrid input, namely *M-VDSR-H*. Specifically, *M-VDSR-H* first extracts underlying features from the LR LF image and HR RGB image separately, which are then combined together and fed into the *VDSR* network. The architecture can be found in the *Supplementary Material*. Note that all the learning-based methods were re-trained over our training datasets for fair comparisons.

Comparisons of Quantitative Results. We used PSNR and SSIM to quantitatively measure the quality of the reconstructed high fidelity LF images by different methods, and the corresponding results are listed in Tables 1 and 2. We can observe that:

- methods with a hybrid input, i.e., *PaSR*, *CrossNet*, *M-VDSR-H* and *Ours*, significantly outperform those with only an LR LF input, i.e., *SAS-conv* and *M-VDSR*, which indicates that the extra HR RGB image indeed makes contribution by providing more high-frequency information about the scene, and the four algorithms have the ability to take advantage of such valuable information to some extent. Also, this observation validates the potential of the hybrid LF imaging;
- among methods with a hybrid input, the non-learning based method *PaSR* is inferior to others, indicating that

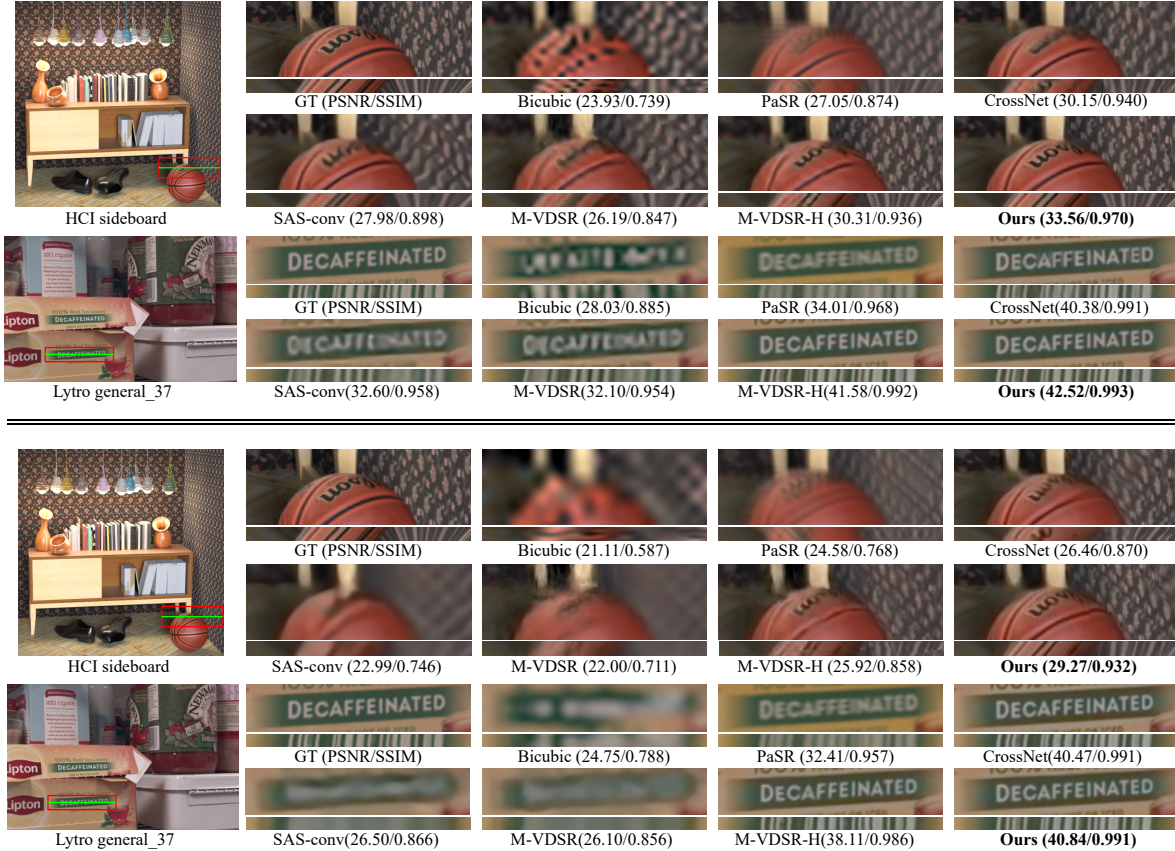


Figure 3. Visual comparisons of different methods on *HCI* and *Lytro* datasets. For each algorithm, we provide the zoom-in images of the red block and EPIs constructed at the green line. The upper and bottom parts correspond to the $4\times$ and $8\times$ reconstruction tasks, respectively. See the *Supplementary Material* for more visual comparisons.

an simple model with a small capacity is not enough to model the intricate relations contained in the hybrid input, while learning-based methods, including *CrossNet*, *M-VDSR-H* and *Ours*, have much larger capacities; and

- our approach achieves the highest PSNR/SSIM at both datasets and scales, which can exceed the second best methods (i.e., *CrossNet* or *M-VDSR-H*) by more than 2 dB, demonstrating the great advantage of our method. Specifically, *M-VDSR-H* simply concatenates the HR RGB image to the LR LF image in feature space, making it difficult to model the geometric relationship between them. *CrossNet* handles SAIs in an LF image independently, so it cannot make use of the valuable complementary information among SAIs and fails to preserve the LF structure. In contrast, our method is able to explicitly characterize and explore the complicated, multi-dimensional, and cross-domain relations of the hybrid input, leading to superior performance.

Comparisons of Visual Results.

We visually compared

different methods for $4\times$ and $8\times$ reconstruction in Fig. 3. These results further demonstrate the significant advantages of the proposed approaches over the state-of-the-art ones, i.e., our approach can reconstruct sharper edges and clearer scenes, which are closer to the ground-truth ones. Particularly, for $8\times$ reconstruction, it is very difficult to recover the details without the guidance of an HR RGB image. From the bottom part of Fig. 3, it can be seen that the patterns in the results of *SAS-conv* and *M-VDSR* are totally destructed. In contrast, *CrossNet*, *M-VDSR-H* and *Ours* accept less influence of the scale increasing and can still produce acceptable results. Moreover, our algorithm successfully preserves the high-frequency details and reconstructs sharper images, which is obvious in *HCI sideboard*.

Comparisons of the LF Structure. The most valuable information of LF data is the LF structure in Eq. 2, which implicitly represents the geometry of the scene/object. Here, we evaluated the LF structure of the reconstructed high-fidelity LF images by different methods both qualitatively and quantitatively. Comparing the 2-D EPI is a straightforward way to evaluate the LF structure qualita-

LF image	SR-Net	WarpNet	Final
Bedroom	37.27/0.976	35.51/0.969	37.35/0.977
Boardgames	36.99/0.984	35.09/0.980	37.84/0.987
Sideboard	29.19/0.932	27.47/0.907	29.27/0.932
Town	35.72/0.972	33.51/0.964	36.09/0.974

Table 3. Effectiveness verification of the fusion component in our approach. We compare the reconstruction quality of the final output and intermediate predictions under the $8\times$ reconstruction task over *HCI*.

	PaSR	CrossNet	SAS-conv	M-VDSR	M-VDSR-H	Ours
HCI $4\times$	4556.61	15.30	3.73	0.29	2.51	6.31
HCI $8\times$	1191.30	15.32	3.89	0.30	2.51	6.54
Lytro $4\times$	2152.14	7.72	1.37	0.13	1.23	2.80
Lytro $8\times$	567.67	7.73	1.43	0.13	1.23	2.88

Table 4. Comparisons of the average running time (in second) of different algorithms for reconstructing a high-fidelity LF image.

tively. In the EPI of a real LF image, the projections of a single scene point observed in different SAIs construct a straight line. Therefore, we present EPIs constructed from the predictions of different algorithms for comparison in Fig. 3. It can be seen that the EPIs of our algorithm have clearer line texture and more accurate slopes, which demonstrates that our network preserves the LF structure better than others. For example, in *Lytro general_37*, although *CrossNet* and *M-VDSR-H* can reconstruct the letters as clear as *Ours*, they fail to reconstruct the correct LF structure, which is reflected by the non-straight EPI lines.

We also quantitatively evaluated the LF structure by using the LF parallax edge precision-recall (PR) curves [6], and Fig. 5 shows the corresponding results, where it can be seen that the PR curves by our methods are closer to the top-right corner than the others, demonstrating that our method preserves the LF parallax best.

Efficiency. We also compared the computational complexities of different methods by measuring the running time (in second) of the testing phase, and Table 4 lists the results. All methods were tested on a desktop with Intel CPU i7-7700@3.60GHz, 64 GB RAM and NVIDIA GeForce GTX 1080 Ti. From Table 4, it can be observed that our approach is much faster than *CrossNet* and *PaSR*, and slightly slower than the others. But taking the trade-off between the computational complexity and reconstruction quality, we believe our method is the best one. In addition, the detailed number of model parameters of our network can be found in the *Supplementary Material*.

4.4. Ablation Study

To validate the effectiveness of the fusion component, we compared the reconstruction quality of the intermediate predictions by SR-Net and WarpNet and the final output under the $8\times$ reconstruction over *HCI*. From Table 3, it can be seen that the PSNR/SSIM values of the final output are higher than those of the intermediate predictions, and es-

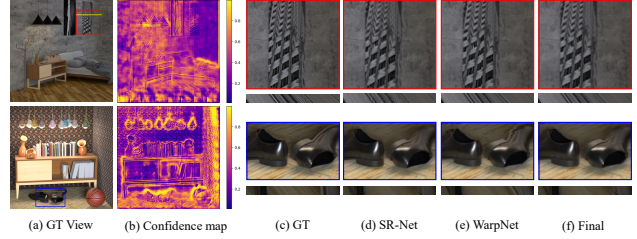


Figure 4. Visual comparisons of intermediate predictions:(a) ground-truth (GT) SAIs, (b) confidence maps by the SR-Net, where a larger value means higher confidence, and zoom-in blocks extracted from the (c) GT SAIs, (d) predictions by the SR-Net, (e) predictions by the WarpNet, and (f) final outputs. *Red* frames in the first row indicate the advantages of WarpNet and *Blue* frames in the second row indicate the advantages of SR-Net.

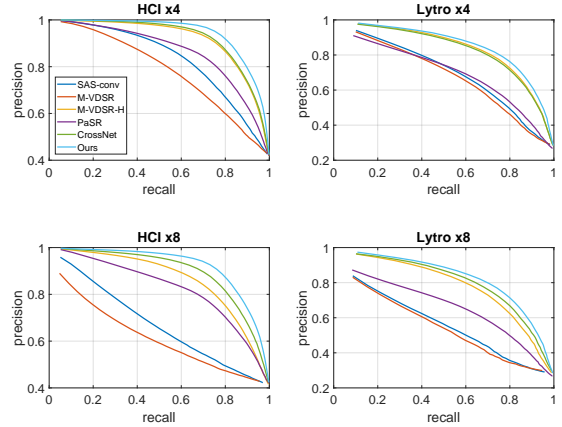


Figure 5. Parallax content PR curves for different methods. The averages across each dataset are presented. All subfigures share the same legend shown in the first one. The PR curve for each individual LF image can be found in the *Supplementary Material*.

pecially on the *Boardgames* image, the PSNR is improved more than 0.8 dB and 2.7 dB with respect to the SR-Net and WarpNet, respectively, demonstrating the effectiveness of the fusion component. To further investigate the difference between SR-Net and WarpNet as well as their contributions to the final output, we visually compared the intermediate predictions and the corresponding confidence maps in Fig. 4. For plain areas (*red* frames in the first row), the prediction of SR-Net is blurred while that of WarpNet has sharper edges. The confidence map also shows that WarpNet has higher confidence in these areas. For areas with discontinuous depth (*blue* frames in the second row), the prediction of WarpNet has distortion while that of SR-Net maintains the content and has higher confidence. Therefore, we can conclude that the fusion is indeed able to leverage the advantages of these two modules. In addition, EPIs in Fig. 4 demonstrate the improvement on the LF structure preservation after the fusion.

5. Discussion

Due to the lack of publicly available real hybrid inputs and the difficulty of building a hybrid imaging system, we only validated the effectiveness and advantages of our framework by using simulated hybrid inputs over synthetic and real LF data. In the following work, we will evaluate it over real hybrid inputs acquired by a typical hybrid imaging system.

In view of the impressive quality achieved in the reconstruction of a large up-sampling scale, we believe our framework could potentially decrease the cost of high-fidelity LF data acquisition for speeding the deployment of LF technique in practice, such as immersive communication. Under this setting, our method can also save the storage cost. In addition, our framework will be potentially beneficial to the compression of LF data directly acquired by other advanced devices, which is an emerging and high desirable issue for LF based immersive communication [14]. For example, at the server side, the spatial resolution of all SAIs except a certain one involved in an LF image can be reduced and likewise the decrease of its data size. And the data can be recovered with our framework at the clients.

6. Conclusion

We have presented a novel learning-based method for reconstructing a high-fidelity LF image from a hybrid input. Owing to the elegant and innovative network architecture, which is capable of comprehensively taking advantage of the underlying properties of the input from two complementary and parallel perspectives, our method not only achieved more than 2 dB improvement in terms of the reconstruction quality and preserved the LF structure much better, but also run in an end-to-end manner and at a high speed, when compared with state-of-the-art approaches.

References

- [1] Lytro illum. <https://www.lytro.com/>. [Online]. 1
- [2] Raytrix. <https://www.raytrix.de/>. [Online]. 1
- [3] R. S. a. G. W. Abhilash Sunder Raj, Michael Lowney. Stanford lytro light field archive. <http://lightfields.stanford.edu/LF2016.html>. [Online]. 6
- [4] V. Boominathan, K. Mitra, and A. Veeraraghavan. Improving resolution and depth-of-field of light field cameras using a hybrid imaging system. In *IEEE International Conference on Computational Photography (ICCP)*, pages 1–10, 2014. 1, 2, 6
- [5] H. Chang, D.-Y. Yeung, and Y. Xiong. Super-resolution through neighbor embedding. In *IEEE Conference on Computer Vision and Pattern Recognition (CVPR)*, pages I–I, 2004. 2
- [6] J. Chen, J. Hou, and L.-P. Chau. Light field denoising via anisotropic parallax analysis in a cnn framework. *IEEE Signal Processing Letters*, 25(9):1403–1407, 2018. 8
- [7] C. Dong, C. C. Loy, K. He, and X. Tang. Image super-resolution using deep convolutional networks. *IEEE Transactions on Pattern Analysis and Machine Intelligence*, 38(2):295–307, 2016. 2
- [8] R. A. Farrugia, C. Galea, and C. Guillemot. Super resolution of light field images using linear subspace projection of patch-volumes. *IEEE Journal of Selected Topics in Signal Processing*, 11(7):1058–1071, 2017. 2
- [9] M. Feng, Y. Wang, J. Liu, L. Zhang, H. F. Zaki, and A. Mian. Benchmark dataset and method for depth estimation from light field images. *IEEE Transactions on Image Processing*, 27(7):3586–3598, 2018. 4
- [10] J. Fiss, B. Curless, and R. Szeliski. Refocusing plenoptic images using depth-adaptive splatting. In *IEEE International Conference on Computational Photography (ICCP)*, pages 1–9, 2014. 1
- [11] S. Heber and T. Pock. Shape from light field meets robust pca. In *European Conference on Computer Vision (ECCV)*, pages 751–767, 2014. 2
- [12] S. Heber, W. Yu, and T. Pock. Neural epi-volume networks for shape from light field. In *International Conference on Computer Vision (ICCV)*, pages 2271–2279, 2017. 4
- [13] K. Honauer, O. Johannsen, D. Kondermann, and B. Goldluecke. A dataset and evaluation methodology for depth estimation on 4d light fields. In *Asian Conference on Computer Vision (ACCV)*, pages 19–34, 2016. 6
- [14] J. Hou, J. Chen, and L.-P. Chau. Light field image compression based on bi-level view compensation with rate-distortion optimization. *IEEE Transactions on Circuits and Systems for Video Technology*, 29(2):517–530, 2019. 9
- [15] F.-C. Huang, K. Chen, and G. Wetzstein. The light field stereoscope: immersive computer graphics via factored near-eye light field displays with focus cues. *ACM Transactions on Graphics*, 34(4):60, 2015. 1
- [16] J.-B. Huang, A. Singh, and N. Ahuja. Single image super-resolution from transformed self-exemplars. In *IEEE Conference on Computer Vision and Pattern Recognition (CVPR)*, pages 5197–5206, 2015. 2
- [17] M. Jaderberg, K. Simonyan, A. Zisserman, et al. Spatial transformer networks. In *Advances in Neural Information Processing Systems (NeurIPS)*, pages 2017–2025, 2015. 5
- [18] J. Johnson, A. Alahi, and L. Fei-Fei. Perceptual losses for real-time style transfer and super-resolution. In *European Conference on Computer Vision (ECCV)*, pages 694–711, 2016. 2
- [19] N. K. Kalantari, T.-C. Wang, and R. Ramamoorthi. Learning-based view synthesis for light field cameras. *ACM Transactions on Graphics*, 35(6):193, 2016. 5, 6
- [20] C. Kim, H. Zimmer, Y. Pritch, A. Sorkine-Hornung, and M. H. Gross. Scene reconstruction from high spatio-angular resolution light fields. *ACM Transactions on Graphics*, 32(4):73–1, 2013. 1
- [21] J. Kim, J. Kwon Lee, and K. Mu Lee. Accurate image super-resolution using very deep convolutional networks. In *IEEE Conference on Computer Vision and Pattern Recognition (CVPR)*, pages 1646–1654, 2016. 2, 6
- [22] W.-S. Lai, J.-B. Huang, N. Ahuja, and M.-H. Yang. Deep laplacian pyramid networks for fast and accurate super-resolution. In *IEEE Conference on Computer Vision and Pattern Recognition (CVPR)*, pages 624–632, 2017. 2, 3
- [23] C. Ledig, L. Theis, F. Huszár, J. Caballero, A. Cunningham, A. Acosta, A. P. Aitken, A. Tejani, J. Totz, Z. Wang, et al. Photo-realistic single image super-resolution using a generative adversarial network. In *IEEE Conference on Computer Vision and Pattern Recognition (CVPR)*, pages 105–114, 2017. 2, 4
- [24] M. Levoy and P. Hanrahan. Light field rendering. In *Proceedings of the 23rd Annual Conference on Computer Graphics and Interactive Techniques*, pages 31–42, 1996. 1
- [25] N. Li, J. Ye, Y. Ji, H. Ling, and J. Yu. Saliency detection on light field. In *IEEE Conference on Computer Vision and Pattern Recognition (CVPR)*, pages 2806–2813, 2014. 1
- [26] C.-H. Lu, S. Muenzel, and J. W. Fleischer. High-resolution light-field microscopy. In *Imaging and Applied Optics*, 2013. 2
- [27] M. Mathieu, C. Couprie, and Y. LeCun. Deep multi-scale video prediction beyond mean square error. *International Conference on Learning Representations (ICLR)*, pages 1–11, 2016. 4
- [28] K. Mitra and A. Veeraraghavan. Light field denoising, light field superresolution and stereo camera based refocussing using a gmm light field patch prior. In *IEEE Conference on Computer Vision and Pattern Recognition Workshops (CVPRW)*, pages 22–28, 2012. 2
- [29] R. Ng, M. Levoy, M. Brédif, G. Duval, M. Horowitz, and P. Hanrahan. Light field photography with a hand-held plenoptic camera. *Computer Science Technical Report*, 2(11):1–11, 2005. 1
- [30] M. Rossi and P. Frossard. Geometry-consistent light field super-resolution via graph-based regularization. *IEEE Transactions on Image Processing*, 27(9):4207–4218, 2018. 1, 2
- [31] P. P. Srinivasan, R. Ng, and R. Ramamoorthi. Light field blind motion deblurring. In *IEEE Conference on Computer Vision and Pattern Recognition (CVPR)*, pages 2354–2362, 2017. 1

- [32] J. Tian and K.-K. Ma. A survey on super-resolution imaging. *Signal, Image and Video Processing*, 5(3):329–342, 2011. 2
- [33] R. Timofte, V. De Smet, and L. Van Gool. A+: Adjusted anchored neighborhood regression for fast super-resolution. In *IEEE Asian Conference on Computer Vision (ACCV)*, pages 111–126, 2014. 2
- [34] T.-C. Wang, A. A. Efros, and R. Ramamoorthi. Occlusion-aware depth estimation using light-field cameras. In *International Conference on Computer Vision (ICCV)*, pages 3487–3495, 2015. 4
- [35] T.-C. Wang, J.-Y. Zhu, E. Hiroaki, M. Chandraker, A. A. Efros, and R. Ramamoorthi. A 4d light-field dataset and cnn architectures for material recognition. In *European Conference on Computer Vision (ECCV)*, pages 121–138, 2016. 1
- [36] T.-C. Wang, J.-Y. Zhu, N. K. Kalantari, A. A. Efros, and R. Ramamoorthi. Light field video capture using a learning-based hybrid imaging system. *ACM Transactions on Graphics*, 36(4):133, 2017. 1, 2
- [37] X. Wang, L. Li, and G. Hou. High-resolution light field reconstruction using a hybrid imaging system. *Applied optics*, 55(10):2580–2593, 2016. 1, 2, 6
- [38] Y. Wang, F. Liu, K. Zhang, G. Hou, Z. Sun, and T. Tan. Lfnet: A novel bidirectional recurrent convolutional neural network for light-field image super-resolution. *IEEE Transactions on Image Processing*, 27(9):4274–4286, 2018. 2
- [39] Y. Wang, Y. Liu, W. Heidrich, and Q. Dai. The light field attachment: Turning a dslr into a light field camera using a low budget camera ring. *IEEE Transactions on Visualization and Computer Graphics*, 23(10):2357–2364, 2017. 1, 2, 6
- [40] Z. Wang, J. Chen, and S. C. Hoi. Deep learning for image super-resolution: A survey. *arXiv preprint arXiv:1902.06068*, 2019. 2
- [41] S. Wanner and B. Goldluecke. Globally consistent depth labeling of 4d light fields. In *IEEE Conference on Computer Vision and Pattern Recognition (CVPR)*, pages 41–48, 2012. 4
- [42] S. Wanner and B. Goldluecke. Variational light field analysis for disparity estimation and super-resolution. *IEEE Transactions on Pattern Analysis and Machine Intelligence*, 36(3):606–619, 2014. 1, 2
- [43] H. W. F. Yeung, J. Hou, X. Chen, J. Chen, Z. Chen, and Y. Y. Chung. Light field spatial super-resolution using deep efficient spatial-angular separable convolution. *IEEE Transactions on Image Processing*, 28(5):2319–2330, 2018. 1, 2, 3, 4, 6
- [44] Y. Yoon, H.-G. Jeon, D. Yoo, J.-Y. Lee, and I. So Kweon. Learning a deep convolutional network for light-field image super-resolution. In *IEEE International Conference on Computer Vision Workshops (ICCVW)*, pages 24–32, 2015. 1, 2
- [45] J. Yu. A light-field journey to virtual reality. *IEEE MultiMedia*, 24(2):104–112, 2017. 1
- [46] Y. Yuan, Z. Cao, and L. Su. Light-field image superresolution using a combined deep cnn based on epi. *IEEE Signal Processing Letters*, 25(9):1359–1363, 2018. 2
- [47] Y. Zhang, Y. Tian, Y. Kong, B. Zhong, and Y. Fu. Residual dense network for image super-resolution. In *IEEE Conference on Computer Vision and Pattern Recognition (CVPR)*, pages 2472–2481, 2018. 2
- [48] M. Zhao, G. Wu, Y. Li, X. Hao, L. Fang, and Y. Liu. Cross-scale reference-based light field super-resolution. *IEEE Transactions on Computational Imaging*, 4(3):406–418, 2018. 1, 2
- [49] H. Zheng, M. Ji, H. Wang, Y. Liu, and L. Fang. Crossnet: An end-to-end reference-based super resolution network using cross-scale warping. In *European Conference on Computer Vision (ECCV)*, pages 87–104, 2018. 2, 6